Petroleum Science 23 (2026) 791–803

Contents lists available at ScienceDirect

Petroleum Science

journal homepage: www.keaipublishing.com/en/journals/petroleum-science

Original Paper

Mechanism and influencing factors of electroosmosis-driven residual water drainage in soft coal seams during coalbed methane recovery

Jun-Qing Guo [a,*], Peng-Hui Liu [a], De-Zhi Sun [b], Chun-Sheng Lu [c,**], Yu-Qing Wang [a], Wei Li [d]

[a] Key Laboratory of In-situ Property-improving for Mining of Ministry of Education, Taiyuan University of Technology, Taiyuan, 030024, Shanxi, China
[b] School of Mechanics and Architecture Engineering, China University of Mining and Technology (Beijing), Beijing, 100083, China
[c] School of Civil and Mechanical Engineering, Curtin University, Perth, 6845, Western Australia, Australia
[d] Bohai Rim Energy Research Institute, Northeast Petroleum University, Qinhuangdao, 066099, Hebei, China

ARTICLE INFO

Article history:
Received 6 July 2025
Received in revised form
18 September 2025
Accepted 20 October 2025
Available online 25 October 2025

Edited by Meng-Jiao Zhou

Keywords:
Soft coal
Water-blocking effect
Electroosmosis
Residual water saturation
Potential gradient

ABSTRACT

Soft coal seams with low porosity are prone to water-blocking during mid to late stages of coalbed methane production, reducing gas recovery. To address this, an electroosmosis-driven drainage strategy was proposed in this paper, based on the charged properties of soft coal in water. Three coal ranks (anthracite, coking coal, and long-flame coal) were tested using a custom electroosmotic drainage device. Electrical properties were characterized, and the effects of potential gradients on drainage were analyzed. Fluorescent particle tracing and Fourier-transform infrared spectroscopy were used to explore residual water migration. It is shown that electroosmosis can significantly enhance drainage across all coal ranks. For coking and long-flame coals, drainage increases with voltage before stabilizing; anthracite exhibits peaked at 4 V/cm. The fluorescent tracing reveals water coalescence and migration. Long-flame coal shows best, linked to optimal higher hydroxyl content and electronegativity. Electroosmotic force, governed by pH, hydroxyl content, and field strength, enables directional water transport. Finally, an engineering design is suggested to reduce water-blocking and enhance coalbed methane recovery.

1. Introduction

The geological conditions of coal seams in China are highly complex, with structurally affected soft coal seams accounting for approximately 60% of the total (Liu et al., 2022; Zhao et al., 2024; Shen et al., 2015). These seams generally exhibit low permeability and limited porosity under *in-situ* stress conditions (Sang et al., 2020). In the later stages of production, high residual water saturation often leads to water-blocking effects, increases flow resistance, obstructing gas migration, and consequently reducing coalbed methane recovery rates (Zhang et al., 2019). Mitigating water-blocking is therefore essential for improving coalbed methane extraction efficiency.

Extensive studies have explored water-blocking mechanisms and mitigation methods. The use of low-field nuclear magnetic resonance has demonstrated that the saturation of bound water decreases with coal rank, weakening water-blocking effects (Liu et al., 2020). It was concluded that the water-blocking primarily results from bound water obstructing gas pathways. Surfactant-based approaches were designed to reduce surface tension and alter coal wettability, thus preventing fluid invasion into micro-fractures (Hu and Wu, 2014; Song et al., 2019). Thermal stimulation was introduced as a method to raise coal seam temperature, lower water viscosity, and enhance molecular mobility (Hu et al., 2023; Shi et al., 2023). While such methods (e.g., surfactants, thermal injection) improve permeability in structurally intact coals, their effectiveness in soft coal seams, characterized by low porosity and more complex water-blocking behavior during mid-to-late production, is still insufficiently understood (Guo et al., 2024).

* Corresponding author.
** Corresponding author.
E-mail addresses: 13753106501@163.com (J.-Q. Guo), C.Lu@curtin.edu.au (C.-S. Lu).

Peer review under the responsibility of China University of Petroleum (Beijing).

https://doi.org/10.1016/j.petsci.2025.10.021

Therefore, considering the soft and loose structure, large specific surface area, and strong electroosmotic responsiveness of soft coal, a method was proposed to reduce residual water saturation through the application of an external electric field, which induces electroosmosis-driven water migration (Guo et al., 2019). The electroosmosis phenomenon was first discovered in 1809 by the observation of water migration from the anode to the cathode through clay particles in a U-shaped tube filled with clay mineral particles and an aqueous solution under a direct current electric field (Reuss, 1809). The linear relationship between the electroosmotic flow rate and the potential gradient was established, which formed the basis for the first successful application of electroosmosis in soft ground stabilization in 1939 (Casagrande, 1949). Subsequently, it was observed that the variation amplitude of oil-water relative permeability in sandstone increased with higher potential gradients (Aggour et al., 1994). The use of an intermittent power supply mode was proposed to effectively improve the distribution of the effective electric potential in soil, reduce electrode corrosion, and enhance drainage uniformity and energy efficiency (Gong and Jiao, 2011). Soil salinity has a significant impact on electro-osmotic drainage, whereby excessively high content leads to increased energy consumption, accelerated electrode corrosion, and intensified electrolysis, thus requiring its control within an optimal range to balance drainage efficiency and energy cost (Li and Gong, 2011). Therefore, research and applications of the electroosmosis method have been primarily concentrated in fields such as soft soil dewatering, petroleum production enhancement, and tailings treatment (Glendinning et al., 2007; Wittle et al., 2011). However, most research on electroosmosis has mostly focused on geomaterials, while related exploration on soft coal remains relatively scarce, particularly regarding the electroosmotic driving mechanism and microscopic water migration pathways. To effectively characterize the variation in residual water migration pathways within coal samples during the electroosmosis process, this study innovatively employs the fluorescent particle tracing technique. A laboratory model test was conducted on a fractured red clay slope under rainfall conditions (Zeng et al., 2023). By spraying fluorescent tracer and utilizing ultraviolet excitation, they successfully achieved non-destructive and visual tracking of water migration pathways. Thus, applying fluorescent particle tracing technology to characterize residual water migration paths is feasible.

To further reveal the universal mechanisms, three coal ranks were selected for experimental investigation. In terms of resource occurrence and production, medium- and high-rank coals (coking coal and anthracite) serve as the main forces in the global commercial development of coalbed methane. In China, high-rank coalbed methane accounts for 90% of the nation's total production (Zhu, 2022). The Qinshui Basin, rich in high-rank coals, exemplified reservoirs with high gas content, strong adsorption, and low permeability (Yang et al., 2025; Wu, 2025). In contrast, low-rank coals (e.g., long-flame coal) offer substantial future potential due to generally higher permeability and growing importance as replacement production targets (Zhang et al., 2025; Huangfu et al., 2019; Jiang and Jin, 2025). To cover the key coal ranks in both current major production areas and potential future regions, this paper selects three typical coal samples of low, medium, and high rank—namely, long-flame coal, coking coal, and anthracite—for investigation. The paper is organized as follows. Following the test of electrical properties, a self-developed experimental apparatus for electroosmotic drainage is used to examine how potential gradients affect the electroosmotic drainage characteristics across these coal ranks. Then, characterization techniques such as fluorescent particle tracing and Fourier-transform infrared spectroscopy are employed to reveal the mechanism by which electroosmosis drives the migration of residual water in coal. Finally, the main findings are summarized.

2. The principle of electroosmosis

Electroosmosis refers to the phenomenon in which a liquid flows directionally relative to the solid surface it contacts under the influence of an electric field (Chen et al., 2001). Its theoretical foundation is based on the electric double layer theory: when a solid surface comes into contact with an electrolyte solution, ionization of surface groups or ion adsorption results in the formation of a fixed charge layer at the interface. This layer further attracts counterions through electrostatic interactions, forming an electric double layer structure composed of a Stern layer and a diffuse layer. Within the diffuse layer, the net charge density per unit volume of the solution is non-zero. Applying an electric field exerts a body force on the ions in this region, thereby driving ion motion and carrying the surrounding liquid, which leads to macroscopic electroosmotic flow, as illustrated in Fig. 1 (Helmholtz, 1879; Zhang et al., 2024). That is, from a macroscopic perspective, the liquid is subjected to an electroosmotic force. The strength of the electroosmotic effect is influenced by various factors, including solid surface properties (such as surface charge density and surface hydrophilicity/hydrophobicity), electrolyte characteristics (e.g., ion concentration and type), interfacial modifications (such as surfactant adsorption), and operational parameters (e.g., electric field strength, temperature, and pH) (Kamble et al., 2022; Delgado et al., 2007).

To investigate the surface electrochemical properties of coal, the zeta potentials of anthracite, coking coal, and long-flame coal were measured using a JS94H microelectrophoresis instrument

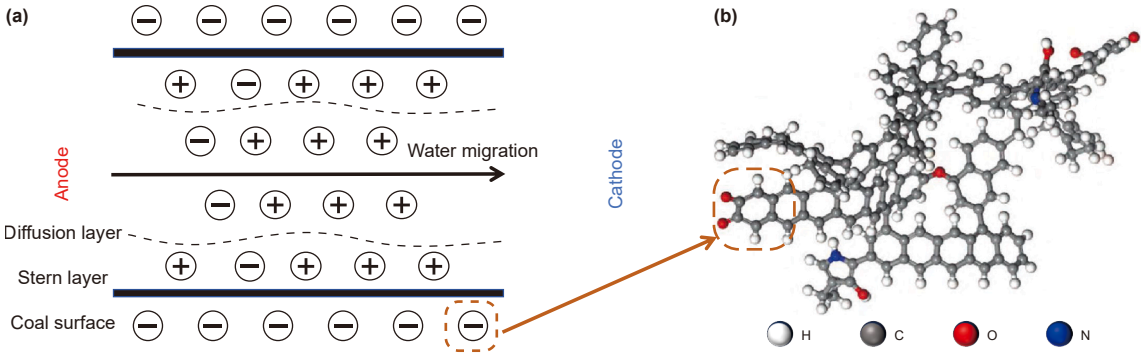

Fig. 1. Schematic illustration of the double electric layer structure with **(a)** the macroscopic structural representation and **(b)** a microscopic molecular model highlighting surface functional groups on coal.

(Powereach Co., China). Platinum electrodes with a switching time of 700 ms were used. Under dry conditions, coal samples were ground and sieved to 200 mesh. A suspension of coal powder and deionized water was sonicated for 2 min and then allowed to settle for 24 h. A 0.5 mL aliquot of the supernatant was introduced into the electrophoresis cell. The focal plane was adjusted to center the crosshair on the screen, and the electrodes were inserted. Experimental parameters including temperature, voltage, and pH were then configured.

Electrophoretic velocities under varying pH conditions were measured, and zeta potential–pH curves were obtained (Fig. 2). All three coal types exhibit electrophoretic behavior. As pH decreases from 11 to 1, the coal surfaces show decreasing electronegativity, eventually transitioning to positive values. This confirms the presence of surface charges. The pH at which the zeta potential equals 0 mV is defined as the isoelectric point. The measured isoelectric points are 1.56 for anthracite, 2.10 for coking coal, and 2.65 for long-flame coal, indicating that anthracite has the lowest electronegativity, followed by coking coal, with long-flame coal exhibiting the highest.

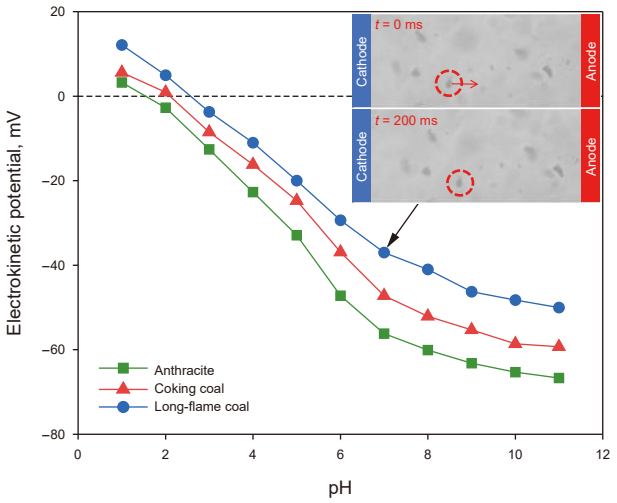

Fig. 2. Zeta potential versus pH curves for anthracite, coking coal, and long-flame coal, where insets show physical diagrams of $t = 0$ ms and $t = 200$ ms.

3. Experiment

3.1. Experimental apparatus

A self-developed electroosmotic drainage apparatus was used, consisting primarily of a DC power supply, ammeter, electroosmotic cylinder, and electrode plates (Fig. 3). The acrylic electroosmotic cylinder measured 80 mm in inner diameter and 120 mm in height was divided equally into anode, intermediate, and cathode zones. The graphite electrodes had an outer diameter of 8 mm, a thickness of 5 mm, and multiple perforations to facilitate fluid flow. A DH1722A-2 DC power supply (Beijing Dahua Radio Instrument Factory) provided an output range of 0–110 V and 0–3 A. Electrical measurements were performed using a PM18 multimeter (Huayi Instruments).

3.2. Experimental samples

Coal rank is a decisive factor governing the physicochemical properties of coal. From low-rank coal (long-flame coal) to medium-rank coal (coking coal) and to high-rank coal (anthracite), systematic evolution is observed in maceral composition, proximate analysis, and ultimate analysis, leading to significant differences in pore structure, molecular configuration, and surface properties (Li et al., 2017). These fundamental disparities further result in distinctly different response mechanisms and effectiveness of coal to external stimuli (Li et al., 2024; Zhu et al., 2024). Therefore, three coal samples of different ranks (anthracite, coking coal, and long-flame coal) were selected for experimental testing. The anthracite was collected from the Sihe Coal Mine (Jincheng, Shanxi, China). The coking coal was obtained from the Sucun Coal Mine (Lvliang, Shanxi, China), while the long-flame coal was sourced from the Suancigou Coal Mine (Ordos, Inner Mongolia, China).

In accordance with GB/T 6948-2008 (Microscopic Determination of Vitrinite Reflectance in Coal), GB/T 212-2008 (Proximate Analysis of Coal), GB/T 476-2001 (Ultimate Analysis of Coal), and GB/T 8899-2013 (Maceral Group and Mineral Composition), the maximum vitrinite reflectance, proximate and ultimate analyses, and maceral composition of the three coal samples were determined. The results are summarized in Table 1.

All coal samples were pulverized and sieved to a particle size of 40–60 mesh (0.3–0.45 mm), then dried in a vacuum oven at

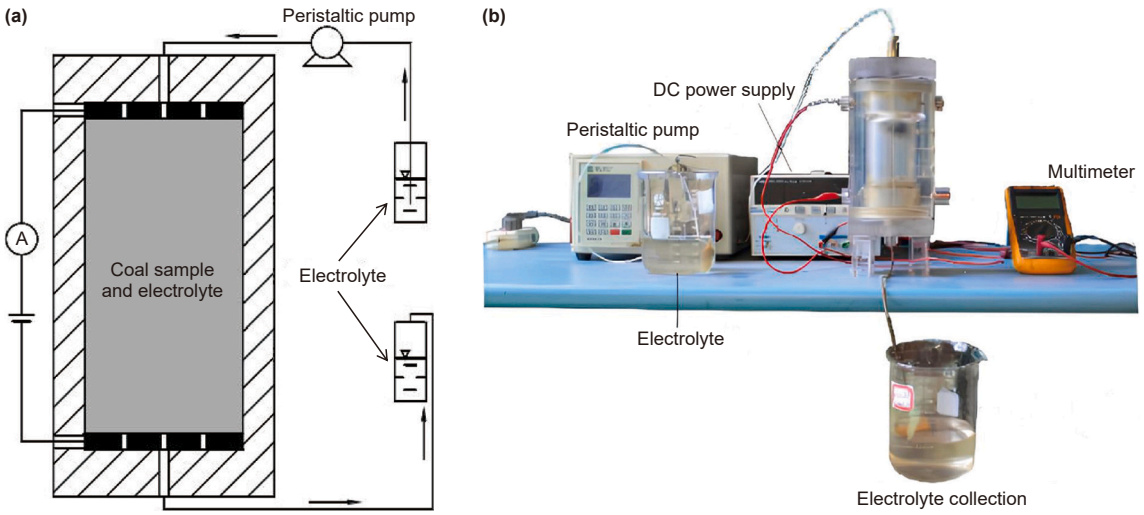

Fig. 3. Experimental setup for electroosmotic drainage in coal with **(a)** schematic diagram and **(b)** its corresponding physical apparatus.

Table 1
Test results for the maximum vitrinite reflectance, proximate analysis, ultimate analysis, and maceral composition of three coal rank samples, where R°_{max} indicates the maximum vitrinite reflectance, and M_{ad}, A_{ad}, and V_{ad} are moisture, ash, and volatile matter on an air-dried basis, respectively.

Coal rank	R°_{max}	Proximate analysis, %			Ultimate analysis, %				Maceral composition analysis, %		
		M_{ad}	A_{ad}	V_{ad}	C	H	O	S	Vitrinite	Inertinite	Exinite
Anthracite	2.51	0.63	8.93	5.38	86.52	2.64	6.83	3.32	66.4	31.3	2.3
Coking coal	1.22	0.24	24.88	24.59	79.23	4.27	2.21	1.76	65.4	30.3	4.3
Long-flame coal	0.60	1.73	16.03	33.09	60.28	3.39	12.99	0.51	53.4	41.3	5.3

105 °C. Samples were weighed every 12 h, and drying was considered complete when the mass change between successive measurements was less than 0.01 g.

3.3. Experimental scheme and procedure

To examine the effects of varying potential gradients on the electroosmotic drainage behavior of coals with different ranks, a series of experiments were conducted using potential gradients of 0, 1, 2, 4, 6, and 8 V/cm. Graphite was chosen as the electrode material due to its chemical stability and conductivity. A mixed electrolyte solution consisting of 0.1 mol/L sodium sulfate and 10% sodium dodecyl sulfate was used to improve both electrolyte infiltration into coal matrix and overall electrical conductivity.

The detailed experimental procedure is as follows:

A geotextile layer was placed at the bottom of the electroosmotic cylinder to prevent loss of coal particles. The cathode electrode plate was positioned on top of the geotextile. The prepared coal sample was then filled and compacted into the cylinder, followed by the placement of the anode electrode plate at the top.

Electrolyte was introduced through the upper inlet. Inflow and outflow volumes were measured at 5 min intervals. Once five consecutive readings showed equal inflow and outflow volumes, full saturation was assumed, and electrolyte injection was stopped.

The bottom outlet was opened to initiate natural drainage. Outflow volumes were recorded every 5 min. This phase concluded when the seepage rate dropped below 0.02 mL/min over a 5-min interval.

After natural drainage, a DC power supply was connected to the electrodes, and a potential gradient of 1 V/cm was applied to induce electroosmotic flow. Outflow was recorded every 5 min until the seepage rate again fell below 0.02 mL/min. The entire process was repeated for potential gradients of 2, 4, 6, 8 V/cm.

3.4. Characterization methods

To enable real-time, in-situ, and visual observation of the migration path variations of residual water at the microscale within coal samples, fluorescent tracer particles were used to visualize electrolyte migration paths. The particles were approximately 600 mesh in size (~0.026 mm), appearing milky white under natural light and emitting a yellowish-green glow under ultraviolet irradiation. The electrolyte composition was consistent with that described previously. To improve visibility of fluorescence, the coal samples were placed in a clear rectangular container (100 mm × 100 mm × 3 mm). Based on the physical experiment, during both natural and electroosmotic drainage tests, the samples were irradiated with ultraviolet light to observe variations in fluorescent area coverage before and after the application of an electric field. A digital single-lens reflex camera was used to capture images. Avizo software was employed for image processing, including threshold segmentation and binarization, to quantify fluorescent area variations, thereby analyzing electrolyte migration patterns across the three coal ranks under different electric field conditions.

A Nicolet iS5 Fourier-transform infrared (FTIR) spectrometer (Thermo Fisher Scientific, USA) was used to characterize surface functional groups of the coal samples. The instrument operated over a wavenumber range of 7800−350 cm^{-1}, with spectral resolution greater than 0.5 cm^{-1}, wavenumber accuracy better than 0.01 cm^{-1}, and a signal-to-noise ratio of 40,000:1. Under dry conditions, coal samples of each rank were mixed with potassium bromide at a 1:150 mass ratio and finely ground in an agate mortar. The mixture was then pressed into pellets under a pressure of 10 MPa. These pellets were analyzed to obtain FTIR spectra, enabling comparison of surface chemical compositions among the different coal ranks.

4. Results and analysis

4.1. Influence of potential gradient on displacement

Fitting of the experimental data on the final drainage volume for the three coal ranks reveals that within the potential gradient range of 0–10 V/cm, the final drainage volume of long-flame coal and coking coal follows a logarithmic pattern, increasing with the rising potential gradient and eventually stabilizing. In contrast, the final drainage volume of anthracite exhibits a parabolic trend, reaching its peak at 4 V/cm. However, the final drainage volume and duration vary across different coal ranks, with specific data presented in Fig. 4 and Table 2. For anthracite, drainage duration extends from 120 min to 230 min, with the final drainage volume increasing from 91.3 mL to 92.3–98.2 mL, representing an improvement of 1.1%–6.9%.

For coking coal, drainage duration increases from 130 min to 160 min, while the final volume rises from 76.1 mL to 82.5–87.0 mL, corresponding to an enhancement of 8.4%–14.3%.

Long-flame coal exhibits the most significant improvement. Drainage duration increases from 110 min to 250 min, and the final volume rises from 74.8 mL to 81.5–94.5 mL, representing a 9.3%–26.3% enhancement.

These differences are attributed to variations in electrokinetic properties among coal ranks. Under neutral aqueous conditions, all three coals exhibit negatively charged surfaces. When an electric field is applied, electroosmotic flow drives residual water toward the cathode, enhancing drainage. However, differences in isoelectric points, reflecting variations in surface charge behavior at a given pH, result in different electroosmotic responses under the same applied field. Lower-rank coals (e.g., long-flame coal) generally possess higher electronegativity, leading to stronger electroosmotic effects and more effective drainage.

As shown in Fig. 5, long-flame and coking coals exhibit drainage volumes that increase with higher potential gradients and eventually plateaus. In contrast, anthracite shows an initial increase in drainage volume, peaking at 4 V/cm, followed by a decline at higher voltages. Specifically, long-flame coal reaches 81.5–94.5 mL across 1–8 V/cm, with drainage enhancements ranging from 9.0% to 26.3%. Coking coal achieves 82.5–87.0 mL, with improvements of 8.4%–14.3%. Anthracite's drainage volume decreases to 92.3–98.2 mL, with reduced enhancement form 6.9% down to 1.1%.

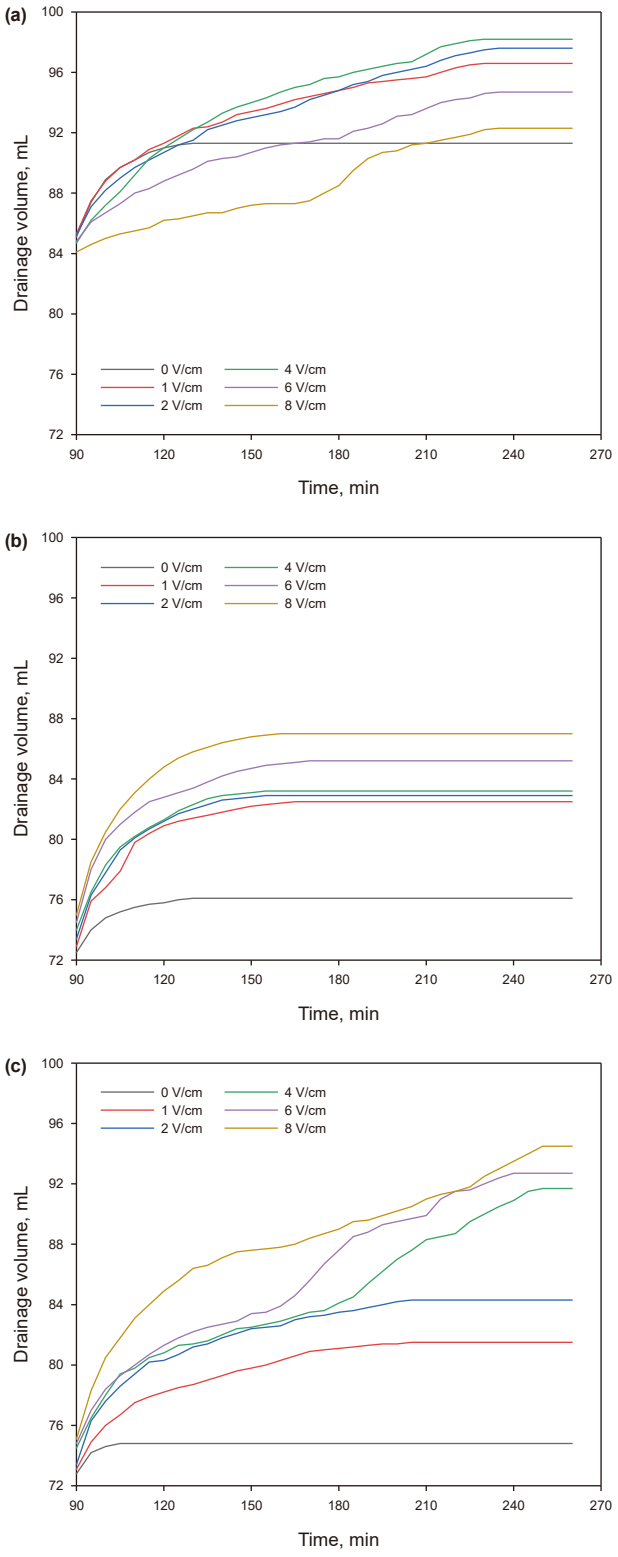

Fig. 4. Drainage volume versus time for three coal ranks under different potential gradients for **(a)** anthracite, **(b)** coking coal, and **(c)** long-flame coal.

This divergence is linked to differences in electronegativity and isoelectric points. Long-flame and coking coals, having higher isoelectric points, maintain strong negative surface charges across the applied voltages, resulting in efficient electroosmotic water transport. However, anthracite, with a lower isoelectric point, experiences anode oxidation at higher voltages (e.g., 8 V/cm), generating excessive H^+ ions that reduces the local pH. This shifts anthracite's surface charge from negative to positive near the anode, reversing the direction of electroosmotic flow and causing water to migrate upward. As a result, water accumulates in the upper region of the anthracite column, while the middle and lower zones dried. In contrast, long-flame and coking coals maintain dry upper and middle zones, with water predominately retained in the lower region.

4.2. Influence of potential gradient on drainage rate

The drainage rates of all three coal ranks exhibit two distinct phases: an initial rapid decline followed by a gradual stabilization, as shown in Fig. 6 and summarized in Table 2. However, the duration and magnitude of these changes vary significantly across the different coal types.

During the rapid drainage phase, the duration remains relatively consistent across tests with or without electric fields: 120 min for anthracite, 110 min for coking coal, and 105 min for long-flame coal. However, drainage rates diverge obviously. For anthracite, the average rates under an electric field change from 0.28 mL/min to a range of 0.14–0.29 mL/min. Coking coal shows enhanced rates, increasing from 0.31 mL/min to 0.45–0.65 mL/min. Long-flame coal exhibits the most significant improvement, with rates rising from 0.27 mL/min to 0.36–0.62 mL/min. These results highlight the rank-dependent effectiveness of electroosmotic drainage.

In the prolonged drainage phase, electric fields substantially extend drainage duration and boost average drainage rates, albeit with some oscillation. Anthracite's duration extends from 15 min to 95–120 min, with rates rising from 0.02 mL/min to 0.05–0.06 mL/min. Coking coal increases from 25 min to 50–65 min, with rates improving from 0.04 mL/min to 0.06–0.09 mL/min. Long-flame coal again shows the highest gains, with duration increasing from 10 min to 110–155 min and drainage rates from 0.04 mL/min to 0.05–0.10 mL/min. The rate fluctuations observed during this phase are attributed to dynamic electroosmotic forces, likely driven by local pH variations during extended drainage.

As shown in Fig. 7(a), during the rapid phase, anthracite's drainage rate remains stable at lower voltages but sharply declines beyond the 4 V/cm threshold. In contrast, coking and long-flame coals exhibit consistent rate increases with rising voltage. Specifically, anthracite rates at 1–8 V/cm range from 0.14 to 0.29 mL/min, maximum decreasing by 50.0%. Coking coal rises to 0.45–0.65 mL/min. Long-flame coal reaches 0.36–0.62 mL/min. In the prolonged drainage phase, as shown in Fig. 7(b), anthracite's rates are 0.05–0.06 mL/min. Coking coal achieves 0.06–0.09 mL/min. Long-flame coal demonstrates the most significant improvement, with rates of 0.05–0.10 mL/min.

These findings further confirm that electroosmotic performance improves with lower coal rank and higher electronegativity, highlighting the practical advantage of applying electric fields for enhanced water removal in soft, low-permeability coals.

4.3. Fluorescent particle tracing

As shown in Fig. 8, fluorescence coverage areas remain nearly unchanged during natural drainage up to 60 min. Following the application of an electric field at 75 min, all three coal ranks display downward expansion of fluorescence coverage, though with distinct spatial and temporal patterns. Anthracite exhibits a rapid initial expansion, followed by oscillatory fluctuations, peaking at 120 min with fluorescence concentrated in the left region. Coking coal shows an initial increase, followed by slight

Table 2
Statistical analysis on electroosmotic drainage testing data of three coal rank coal samples.

Coal rank	Potential gradient, V/cm	Final drainage volume, mL	Drainage rate, mL/min		Drainage durations, min		
			Rapid	Prolonged	Total	Rapid	Prolonged
Anthracite	0	91.3	0.28	0.03	125	120	15
	1	96.6	0.29	0.05	235	120	115
	2	97.6	0.27	0.06	240	120	120
	4	98.2	0.28	0.06	215	120	95
	6	94.7	0.22	0.05	240	120	120
	8	92.3	0.14	0.05	240	120	120
Coking coal	0	76.1	0.31	0.04	135	110	25
	1	82.5	0.45	0.07	170	110	60
	2	82.9	0.52	0.07	160	110	50
	4	83.2	0.53	0.07	160	110	50
	6	85.2	0.60	0.06	175	110	65
	8	87.0	0.65	0.09	165	110	55
Long-flame coal	0	74.8	0.27	0.04	115	105	10
	1	81.5	0.36	0.05	215	105	110
	2	84.3	0.46	0.06	215	105	110
	4	90.7	0.46	0.08	260	105	155
	6	92.7	0.62	0.09	260	105	155
	8	94.5	0.49	0.10	250	105	145

contraction, reaching a peak at 180 min with changes centered in the middle region. In contrast, long-flame coal demonstrates continuous expansion, peaking at 240 min, predominantly in the right region. These observations confirm that electroosmosis induces significant residual water migration in all coal ranks.

To quantitatively assess the dynamic evolution of fluorescent particles, Avizo software was used for threshold segmentation and binarization of the images in Fig. 8. The results, presented in Fig. 9, reveal a transition from discrete punctate fluorescence to aggregated flaky regions under electric fields. New punctate regions gradually emerge and interconnect, forming larger continuous zones. This coalescence and downward movement of fluorescent areas reflect the progressive migration of residual water.

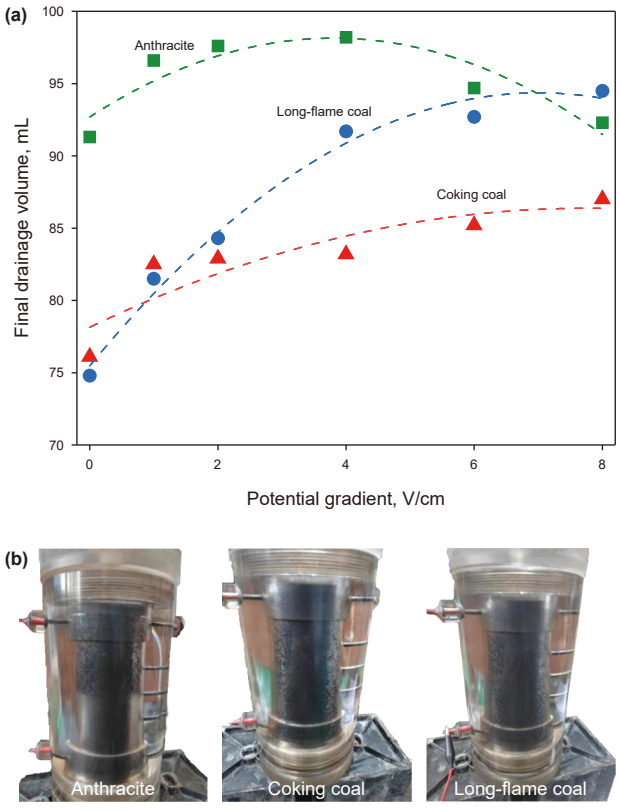

Fig. 5. **(a)** The final displacement versus potential gradients (anthracite, $R^2 = 0.811$; coking coal, $R^2 = 0.949$; long-flame coal, $R^2 = 0.984$) and **(b)** their corresponding physical images at a potential gradient of 8 V/cm.

The frequency distribution curves in Fig. 10 further support this trend: the number of discrete punctate units declines, while the maximum coverage of flaky regions increases after electroosmosis. Table 3 summarizes the temporal changes in fluorescence coverage. Total coverage increases from 17.9%, 11.4%, and 8.9% to 21.3%–26.3%, 11.7%–14.3%, and 9.9%–13.4% for anthracite, coking coal, and long-flame coal, respectively, corresponding to enhancements of 19.0%–46.9%, 2.6%–25.4%, and 11.2%–50.6%. These findings highlight the effectiveness of electroosmosis in mobilizing residual water, with long-flame coal showing the most pronounced response, which is consistent with the drainage performance trends observed.

4.4. Characterization of surface groups

As shown in Fig. 11, the FTIR spectra of the three coal samples exhibit similar peak positions but with varying intensities, suggesting that while the types of functional groups are generally consistent, their concentrations differ significantly among the coal ranks.

It is established that hydroxyl (–OH) groups are the primary contributors to coal surface electronegativity, with larger peak areas corresponding to stronger negative surface charges (Wang et al., 2004). An established method was employed to analyze the hydroxyl region (3000–3600 cm^{-1}) for the quantification of surface –OH content (Ibarra et al., 1996). The resulting peak areas are 61.91 for anthracite, 90.86 for coking coal, and 105.04 for long-flame coal, indicating that lower-rank coals contain higher hydroxyl content. This supports the conclusion that long-flame coal exhibits the greatest surface electronegativity among the three, aligning with its superior electroosmotic performance observed in previous experiments.

5. Discussion

5.1. Underlying mechanisms

Coal is composed primarily of large aromatic rings with aliphatic side chains and condensed structures, whose skeletons are formed by carbon atoms. As the degree of coalification

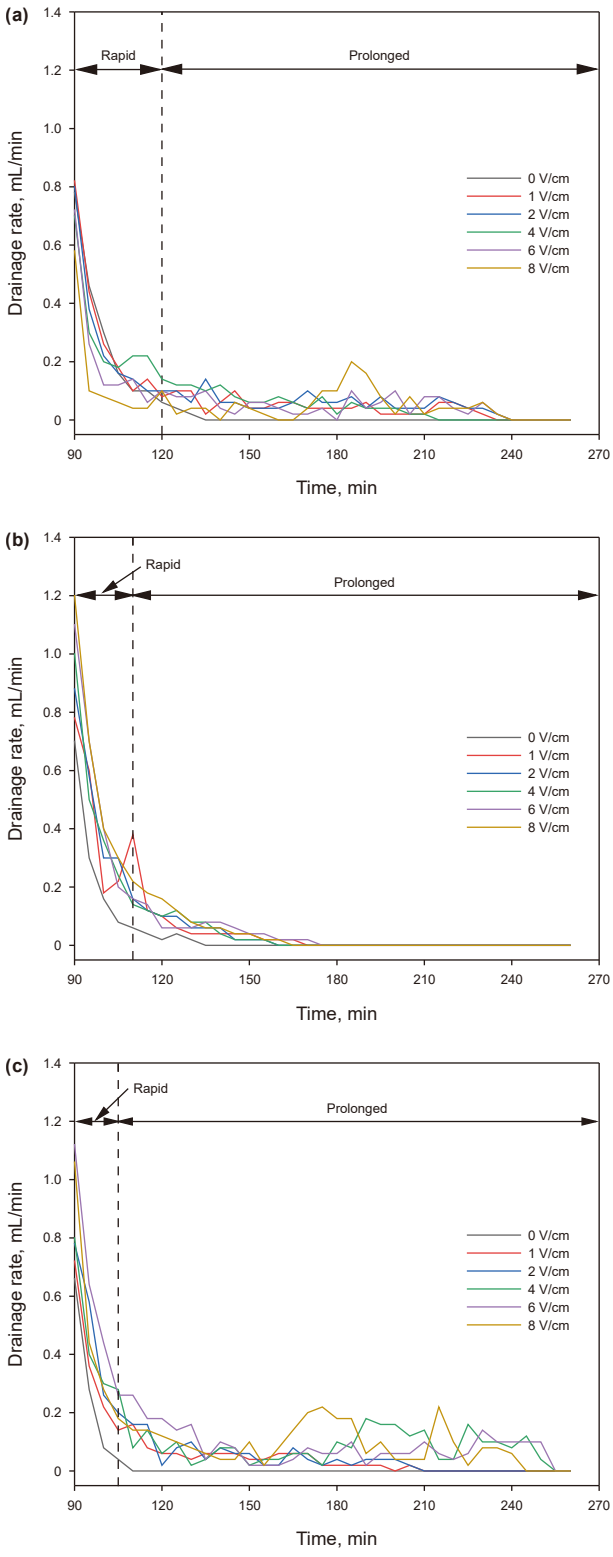

Fig. 6. Variation curves of drainage rate for three coal rank samples under different potential gradients with time for **(a)** anthracite, **(b)** coking coal, and **(c)** long-flame coal.

increases, the carbon content rises, while the hydrogen and oxygen contents decrease, and the nitrogen content slightly decreases (Cheng et al., 2017). The three coal samples selected in this study all belong to organic sedimentary rocks. Their basic structural units are organic macromolecular systems composed of aromatic rings and aliphatic side chains, which collectively exhibit a certain electronegativity, providing the fundamental conditions for electroosmotic effects to occur under an electric field. Meanwhile, depending on the degree of coalification and metamorphic stage, the electronegativity of the three coal samples shows a characteristic pattern of variation (Yang et al., 2021; Zhang et al., 2020; Wang et al., 2016): Long-flame coal exhibits the strongest electronegativity and ion exchange capacity due to its abundant oxygen-containing functional groups (such as hydroxyl groups); the electronegativity of coking coal is moderate; while anthracite, owing to its high aromatization and lack of functional groups, is the weakest overall.

A force analysis of residual water within coal particle voids shows that, as shown in Fig. 12(a), in the absence of an electric field, water retention is primarily governed by a balance between the downward gravitational force gradient and the opposing capillary force, resulting in scattered and localized water retention within the inter-particle voids. When an external electric field is applied, the electronegative characteristics of the coal surface lead to adsorption/ionization and ion diffusion, forming a Stern layer and a diffuse layer near the surface. Within the diffuse layer, the net charge density of the residual water per unit volume is non-zero. The applied electric field exerts a body force on the ions therein, thereby driving ion movement and facilitating the migration of adjacent residual water (Zhang et al., 2024). This provides an electroosmotic force that promotes water movement, consequently modifying the net force acting on the water and enabling the coalescence and directional flow of previously dispersed water, as shown in Fig. 12(b). Moreover, the electroosmotic force is proportional to the potential gradient. Simultaneously, the electroosmotic force is also influenced by coal rank, specifically the surface electronegativity of the coal. Long-flame coal exhibits the strongest electronegativity, followed by coking coal, while anthracite is the weakest. Hence, under the same potential gradient, the electroosmotic force acting on the residual water is highest in long-flame coal, moderate in coking coal, and weakest in anthracite.

Over time, the electric field alters the pH of the surrounding electrolyte. For coals where the pH drops below their isoelectric point (e.g., anthracite), residual water tends to migrate upward. In contrast, when the pH exceeds the isoelectric point (as in coking and long-flame coals), water migration occurs in the downward direction. Long-flame coal demonstrates superior migration efficiency due to its higher hydroxyl content and greater surface electronegativity.

This mechanism can be further explained using the electric double layer theory, as shown in Fig. 12(c). When pH is below the isoelectric point, H^+ ions dominate adsorption in the Stern layer, creating a positively charged inner region. The adjacent diffuse layer becomes negatively charged through counterion adsorption, forming an inner-positive/outer-negative electric double layer. In this configuration, hydrated anions in the diffuse layer migrate upward under the electric field, driving upward water transport in anthracite. Conversely, when pH exceeds the isoelectric point, deprotonation of hydroxyl groups or dissociation of negatively charged functional groups leads to a negatively charged Stern layer, while the diffuse layer attracts cations. This results in an inner-negative/outer-positive electric double layer structure, where hydrated cations migrate downward under the electric field, promoting downward water movement in coking and long-flame coals. The elevated hydroxyl content and surface

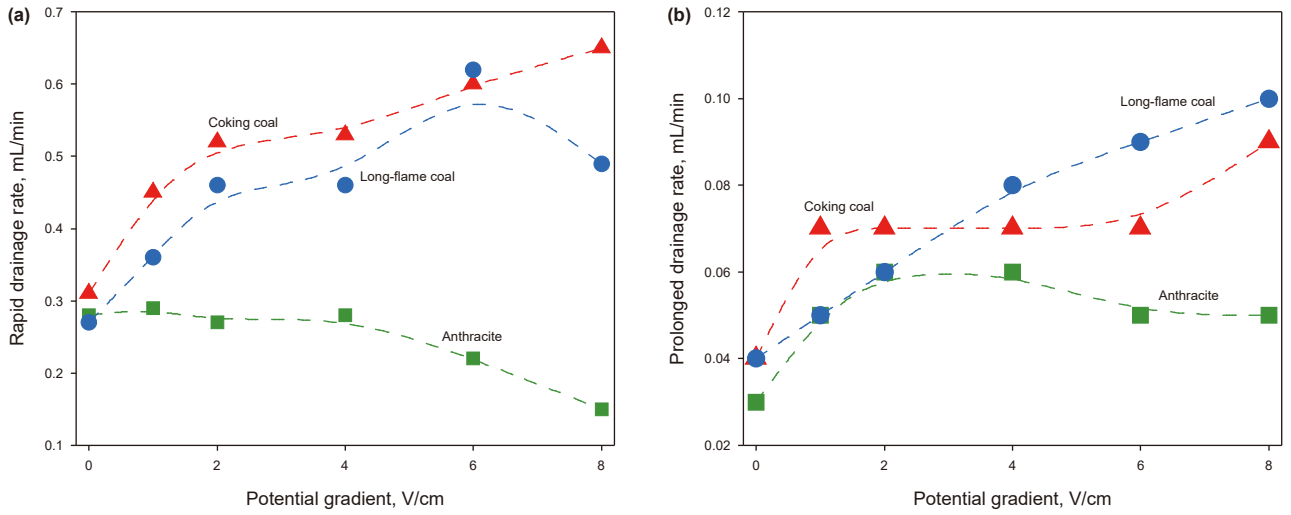

Fig. 7. Average drainage rate versus potential gradient during **(a)** the rapid drainage phase and **(b)** the prolonged drainage phase for anthracite, coking coal, and long-flame coal.

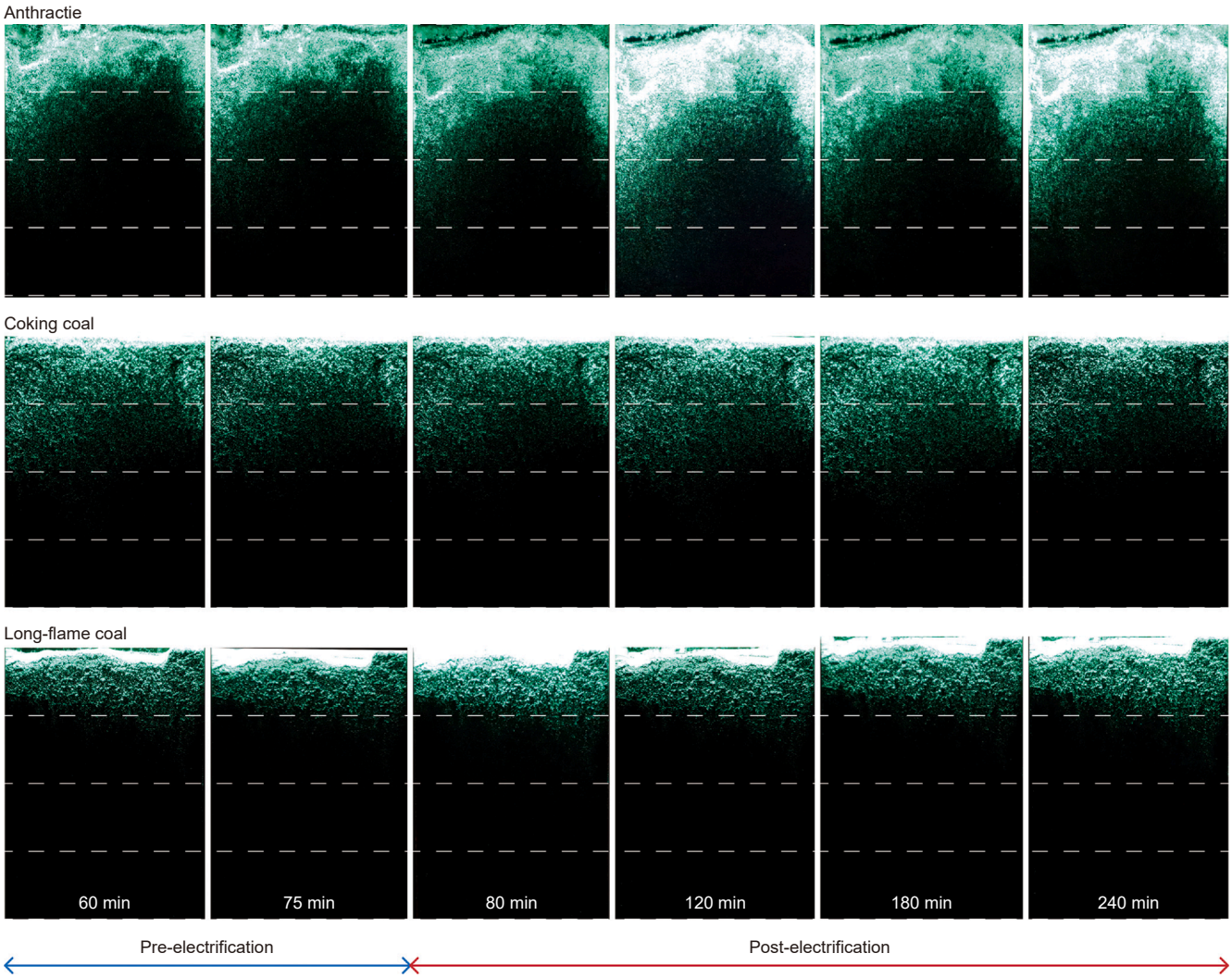

Fig. 8. Fluorescent particle tracing images of three coal ranks, where white dashed lines serve as reference baselines to divide the images into quadrants for visualizing fluorescent area variations.

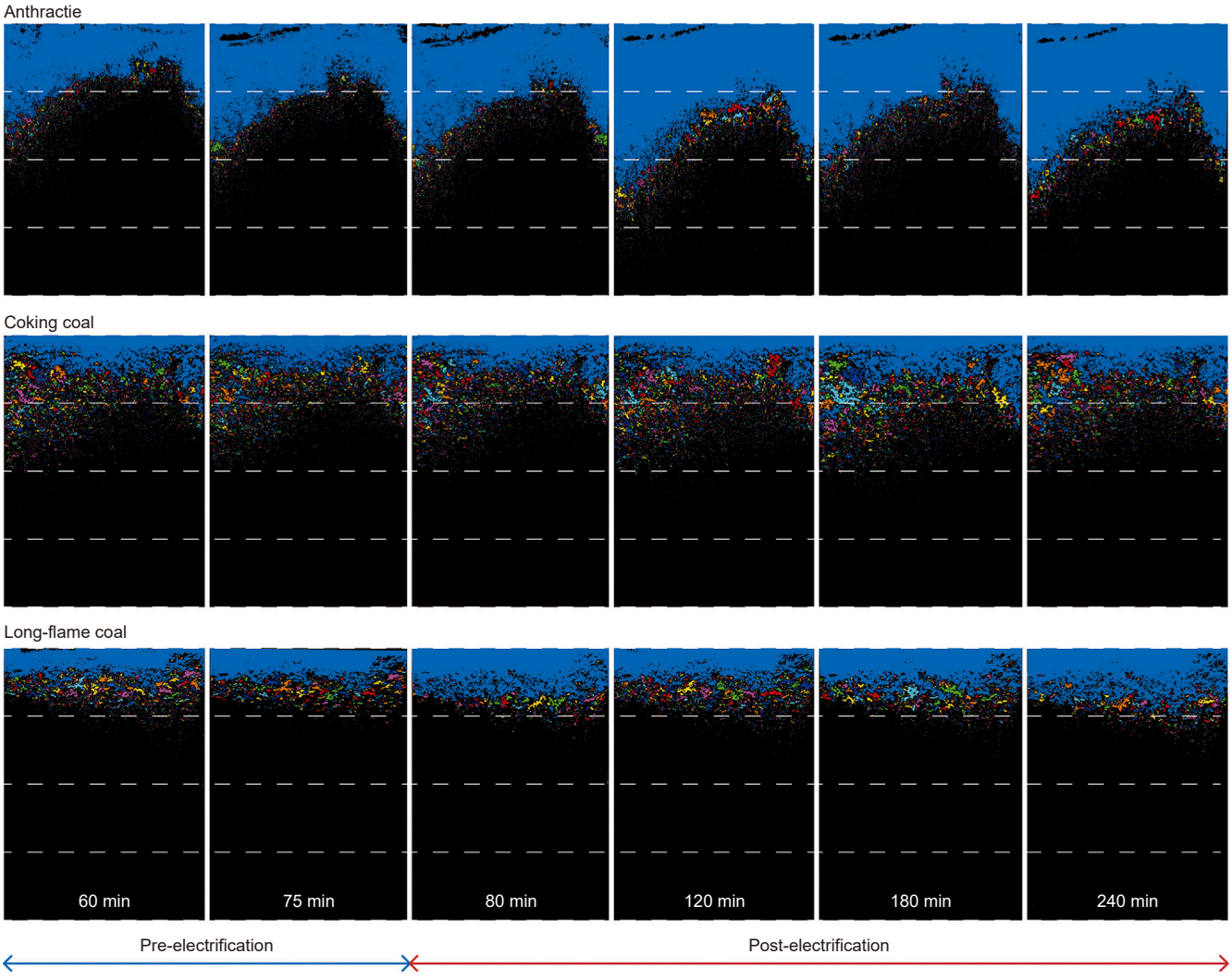

Fig. 9. Binarized fluorescence tracer images for three coal ranks, where white dashed lines indicate reference baselines used to divide the images into quadrants to highlight changes in fluorescent areas.

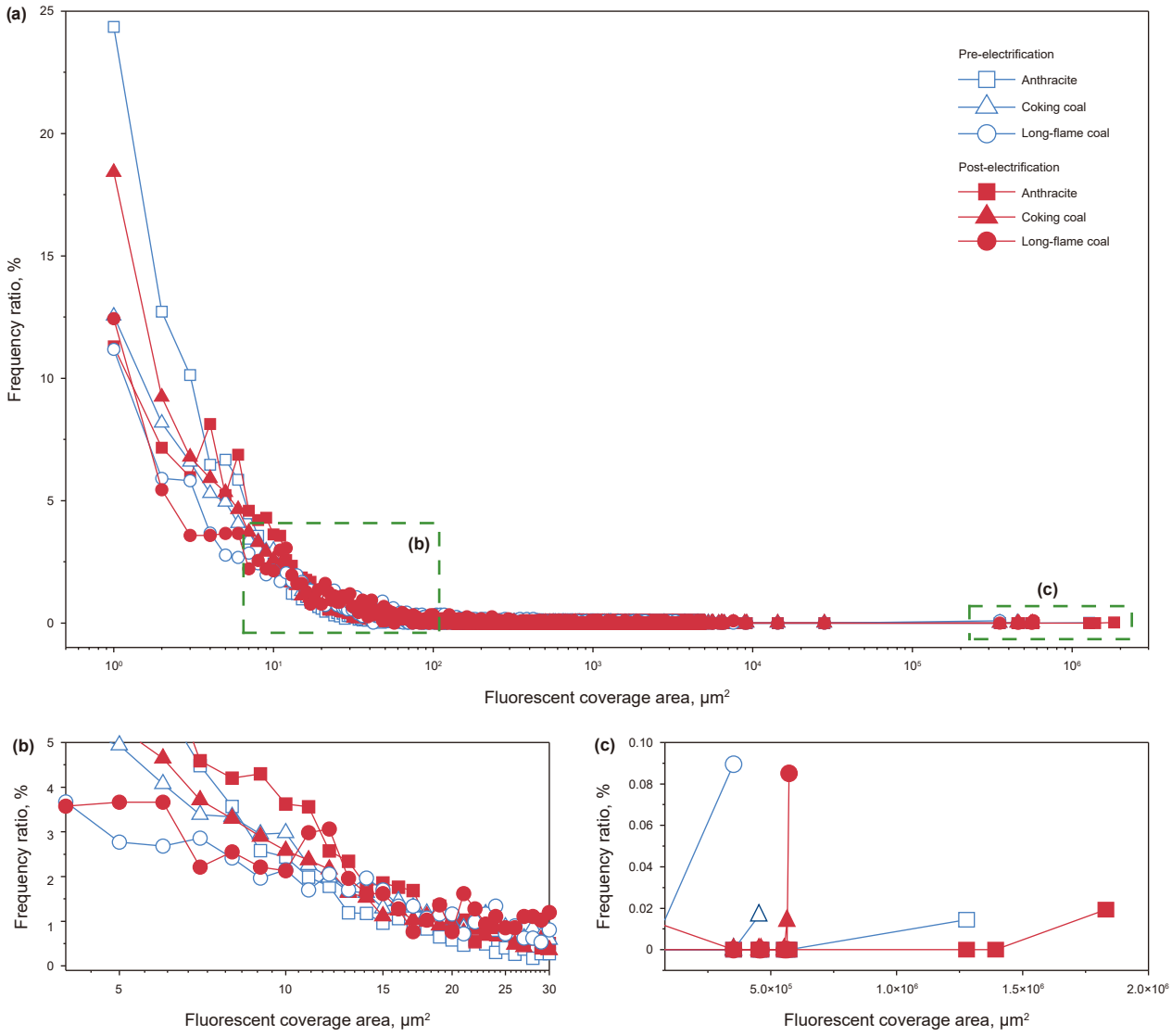

Fig. 10. **(a)** The frequency ratios of three coal samples versus with the fluorescence area, where **(b)** and **(c)** show enlarged views of the two selected regions.

Table 3
Binarization data of fluorescence areas in three types of coal gradation samples.

Coal	Power supply situation	Time, min	Fluorescent coverage area, mm^2	Total area, mm^2	Proportion, %
Anthracite	Pre-electrification	60	1.38	8.10	17.08
		75	1.35	6.88	19.57
	Post-electrification	80	1.49	7.01	21.26
		120	1.98	7.27	27.21
		180	1.69	7.43	22.81
		240	1.93	7.22	26.66
Coking coal	Pre-electrification	60	0.75	6.21	12.12
		75	0.71	6.20	11.44
	Post-electrification	80	0.71	6.32	11.20
		120	0.76	6.03	12.58
		180	0.89	6.25	14.29
		240	0.79	6.02	13.05
Long-flame coal	Pre-electrification	60	0.44	4.96	8.90
		75	0.44	5.00	8.85
	Post-electrification	80	0.61	4.94	12.40
		120	0.49	4.98	9.85
		180	0.56	5.02	11.13
		240	0.65	5.01	13.03

electronegativity of long-flame coal further enhance electroosmotic flow, yielding more efficient water migration.

5.2. Engineering expectation

Based on the electroosmosis-driven water migration mechanisms identified, an engineering strategy can be proposed to reduce residual water saturation, mitigate water-blocking effects, and enhance coalbed methane recovery, as illustrated Fig. 13. A network of vertical wells is first established, with iron anode electrodes installed at injection wellheads and iron cathode electrodes placed at the bottoms of production wells. Fracturing fluids containing electrolytes are then injected into the coal seams to create a conductive environment conducive to electroosmosis.

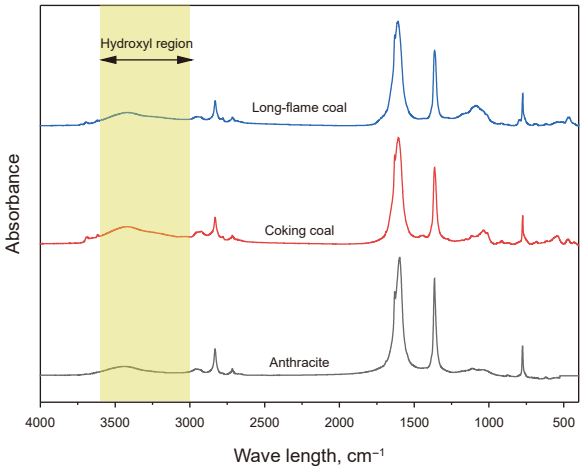

Fig. 11. The FTIR spectra of anthracite, coking coal, and long-flame coal.

During mid-to-late stages of production, when drainage and gas output typically decline, the system is activated by applying an external power source. The resulting electroosmotic force drives the residual water directionally from the injection wells (anode zones) toward the production wells (cathode zones). This directional water migration not only relieves water-blocking effects but also facilitates methane desorption and flow, thereby synergistically improving overall coalbed methane recovery.

Experimental findings suggest that optimal potential gradients vary depending on coal rank. For a typical well spacing of 200 m, high-rank coals (e.g., anthracite) require an applied voltage of 60–100 kV, while medium- and low-rank coals (e.g., coking and long-flame coals) require higher voltages in the range of 140–180 kV.

Existing experimental studies have indicated that, in addition to well location and structural geology, the productivity of high-, medium-, and low-yielding CBM wells, as well as drainage wells, is also controlled by drainage conditions. Reducing residual water saturation can effectively enhance coalbed methane recovery (Liu et al., 2013). Based on high-pressure isothermal adsorption tests under different moisture conditions in deep coal rocks, it was found that for every 1% increase in moisture content, the maximum adsorption capacity of methane decreases by an average of 1.82 m^3/t (Zhou et al., 2025). The application of high-power ultrasound technology to coal seams was shown to enhance drainage efficiency, sustaining effective drainage for over 40 days and resulting in an increase in methane production per well by approximately 3.83 times (Liu et al., 2022). In this study, the application of an external electric field-induced electroosmotic effect promoted water migration, resulting in increased drainage volumes across the three coal ranks by 6.9%–26.3%. Compared with existing methods, electroosmosis offers a promising alternative for field-scale coalbed methane recovery enhancement.

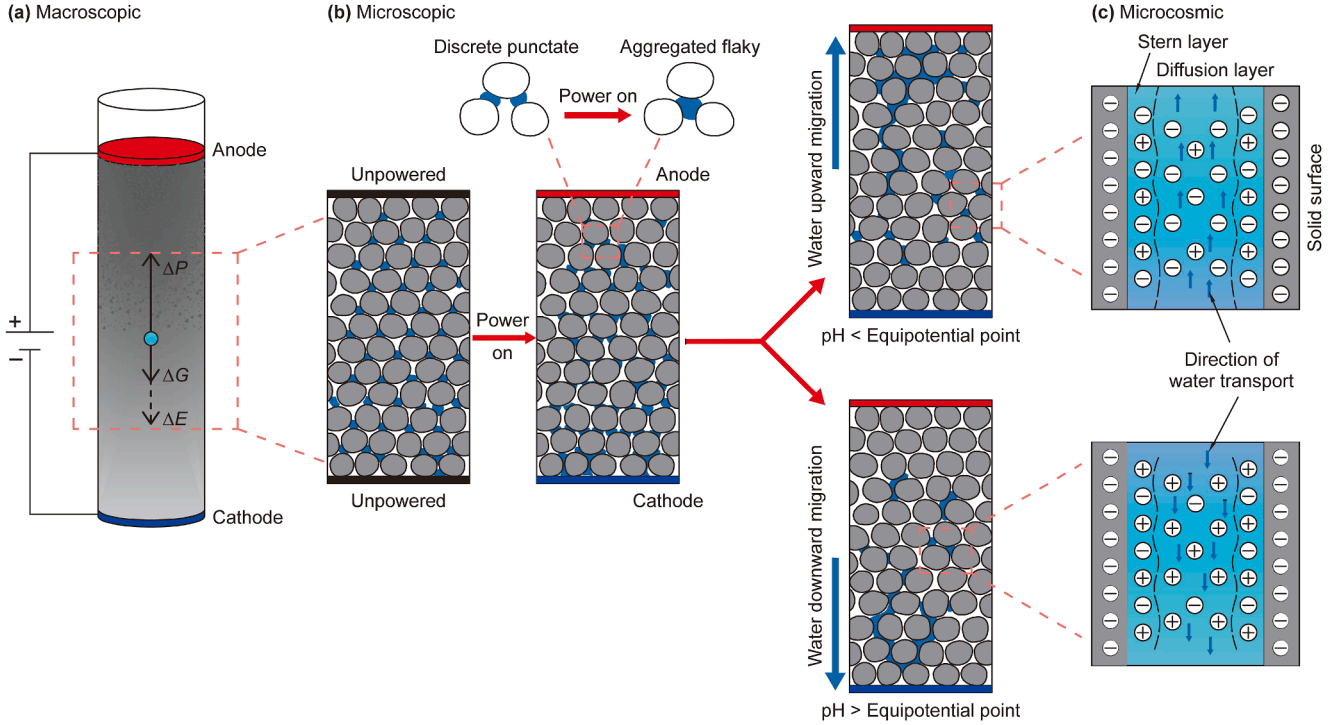

Fig. 12. Schematic illustration of the drainage mechanism for anthracite, coking coal, and long flame coal, where ΔP denotes the opposing capillary force, ΔG the downward gravitational force, and ΔE the additional electroosmotic force.

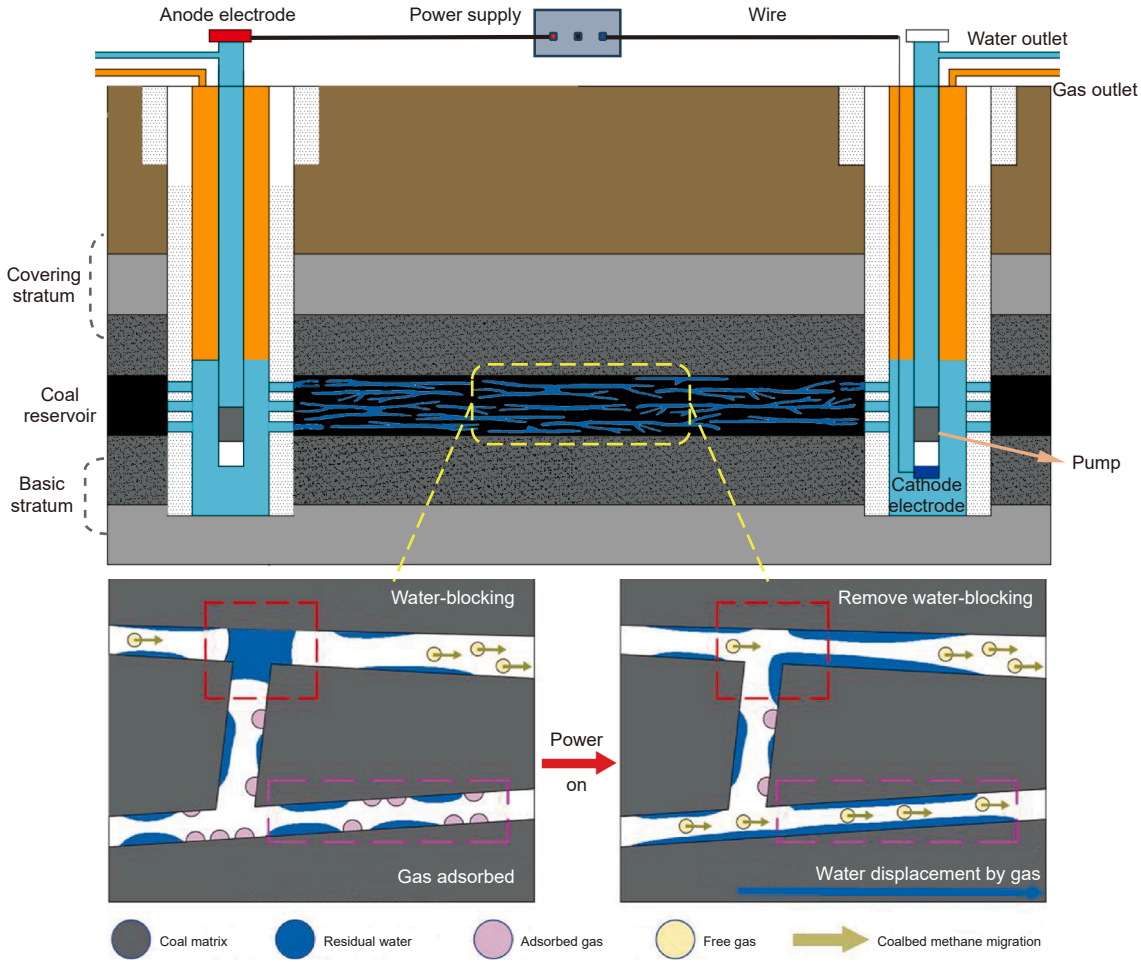

Fig. 13. Engineering design schematic for promoting residual water drainage from soft coal during coalbed methane extraction via electroosmosis.

6. Conclusions

In this paper, we have demonstrated that electroosmosis, induced by externally electric fields, can effectively promote water migration and reduce residual water saturation in coal samples. The efficacy of this process varies significantly across coal ranks, offering a promising strategy to enhance coalbed methane recovery. The main findings are summarized as follows.

(1) After electric field application, the drainage volumes of anthracite, coking coal, and long-flame coal particles were significantly enhanced by electroosmosis, with the maximum increment exceeding a quarter. These improvements are accompanied by substantial extensions in drainage duration, particularly during the prolonged drainage phase. For coking and long-flame coals, drainage volume and rate increase with higher potential gradients before stabilizing. In contrast, anthracite peaks at 4 V/cm and declines thereafter. These differences stem from coal-rank-dependent isoelectric points and dynamic changes in zeta potential driven by pH variation during electroosmosis.

(2) Fluorescent particle tracing reveals a transition from scattered punctate patterns to aggregated flaky distributions across all coal ranks under electric fields. The progressive coalescence and downward migration of residual water are confirmed, with long-flame coal demonstrating the most significant enhancement due to its higher hydroxyl group content and stronger electronegativity.

(3) The mechanism of electroosmotic drainage is further clarified. In the absence of an electric field, residual water is governed by gravitational and capillary forces. With electroosmosis, an additional driving force is introduced, whose direction and strength depend on the solution pH, hydroxyl group concentration, and applied potential gradient. When the pH is below the isoelectric point, water migrates counter to the electric field; when above, migration aligns with it.

CRediT authorship contribution statement

Jun-Qing Guo: Writing – review & editing, Methodology, Conceptualization. **Peng-Hui Liu:** Writing – original draft, Data curation. **De-Zhi Sun:** Data curation. **Chun-Sheng Lu:** Writing – review & editing, Supervision. **Yu-Qing Wang:** Data curation. **Wei Li:** Supervision.

Availability of data and materials

The data and materials that support the findings of this study are available from the corresponding author upon request.

Declaration of competing interests

The authors declare that they have no known competing financial interests or personal relationships that could have appeared to influence the work reported in this paper.

Acknowledgements

This research is financially supported by the National Natural Science Foundation of China (42472238) and the Applied Basic Research Project of Shanxi Province, China (20210302123148).

References

Aggour, M.A., Tchelepi, H.A., Al-Yousef, H.Y., 1994. Effect of electroosmosis on relative permeabilities of sandstones. J. Pet. Sci. Eng. 11 (2), 91–102. https://doi.org/10.1016/0920-4105(94)90031-0.

Casagrande, I.L., 1949. Electroosmosis in soils. Geotechnique 1 (3), 159–177. https://doi.org/10.1680/geot.1949.1.3.159.

Chen, Z.Q., Wang, G.X., Xu, G.Y., 2001. Colloid and Interface Chemistry. Higher Education Press, Beijing.

Cheng, Y.P., Liu, Q.Q., Ren, Y.X., 2017. Coal Mechanics. Science Press, Beijing.

Delgado, A.V., Gonzalez-Caballero, F., Hunter, R.J., et al., 2007. Measurement and interpretation of electrokinetic phenomena. J. Colloid Interface Sci. 309 (2), 194–224. https://doi.org/10.1016/j.jcis.2006.12.075.

Glendinning, S., Lamont-Black, J., Jones, C.J.F.P., 2007. Treatment of sewage sludge using electrokinetic geosynthetics. J. Hazard. Mater. 139 (3), 491–499. https://doi.org/10.1016/j.jhazmat.2006.02.046.

Gong, X.N., Jiao, D., 2011. Experimental study on electro-osmotic consolidation of soft clay under intermittent current condition. J.Cent. South Univ. 42 (6), 1725–1730.

Guo, H.J., Yu, Y.J., Wang, Y.H., et al., 2024. Experimental study on the desorption law and diffusion kinetic characteristics of gas in raw coal and tectonic coal. Energy 289, 129924. https://doi.org/10.1016/j.energy.2023.129924.

Guo, J.Q., Kang, T.H., Kang, J.T., et al., 2019. Research progress of electrokinetic dynamics of rock and fluid. Chin. J. Rock Mech. Eng. 38 (3), 511–526. https://doi.org/10.13722/j.cnki.jrme.2018.0790.

Helmholtz, H., 1879. Studien über elektrische grenzschichten. Ann. Phys. 243 (7), 337–382 (in German).

Hu, L.J., Feng, Z.C., Zhou, D., et al., 2023. Numerical simulation study and engineering practice of in-situ heat injection mining of coalbed methane. J. China Coal Soc. 48 (12), 4473–4486. https://doi.org/10.13225/j.cnki.jccs.2023.0457.

Hu, Y.L., Wu, X.M., 2014. Research on coalbed methane reservoir water blocking damage mechanism and anti-water blocking. J. China Coal Soc. 39 (6), 1107–1111. https://doi.org/10.13225/j.cnki.jccs.2013.1024.

Huangfu, Y.H., Kang, Y.S., Deng, Z., et al., 2019. Low coal rank coalbed methane accumulation model and exploration direction. Acta Pet. Sin. 40 (7), 786–797. https://doi.org/10.7623/syxb201907003.

Ibarra, J., Muñoz, E., Moliner, R., 1996. FTIR study of the evolution of coal structure during the coalification process. Org. Geochem. 24 (6), 725–735. https://doi.org/10.1016/0146-6380(96)00063-0.

Jiang, W.P., Jin, X.L., 2025. Discussion on the influence of coal body structure on the characteristics of methane adsorption/desorption and production in low-rank coal. Coal Sci. Technol. 1–12. https://link.cnki.net/urlid/11.2402.td.20250825.1436.008.

Kamble, S., Agrawal, S., Cherumukkil, S., 2022. Revisiting zeta potential, the key feature of interfacial phenomena, with applications and recent advancements. ChemistrySelect 7 (1), e202103084. https://doi.org/10.1002/slct.202103084.

Li, J., Zhang, J.J., Xiao, Q.L., et al., 2024. Experimental study on differential thermal response and pore-fracture structure evolution characteristics of coals under microwave irradiation: A case study of five different rank coals. Energy Fuel. 38 (11), 9497–9514. https://doi.org/10.1021/acs.energyfuels.4c01228.

Li, Y., Cao, D.Y., Wu, P., et al., 2017. Variation in maceral composition and gas content with vitrinite reflectance in bituminous coal of the eastern Ordos Basin, China. J. Pet. Sci. Eng. 149, 114–125. https://doi.org/10.1016/j.petrol.2016.10.018.

Li, Y., Gong, X.N., 2011. Experimental study on effect of soil salinity on electro-osmotic dewatering in soft clay. Chin. J. Geotech. Eng. 33 (8), 1254–1259 https://doi.org/CNKI:SUN:YTGC.0.2011-08-020.

Liu, D.M., Yao, Y.B., Yuan, X.H., et al., 2022. Experimental evaluation of the dynamic water-blocking effect in coalbed methane reservoir. J. Pet. Sci. Eng. 217, 110887. https://doi.org/10.1016/j.petrol.2022.110887.

Liu, H.H., Sang, S.X., Michael, F., et al., 2013. Production characteristics and drainage optimization of coalbed methane wells: A case study from low-permeability anthracite hosted reservoirs in southern Qinshui Basin, China. Energy Sustain. Dev. 17 (5), 412–423. https://doi.org/10.1016/j.esd.2013.04.005.

Liu, P., Fan, L., Li, Q.G., et al., 2022. Power ultrasound assisted coalbed methane enhancement recovery: field application and performance evaluation in underground coal mine. Fuel 324 (A), 124575. https://doi.org/10.1016/j.fuel.2022.124575.

Liu, Q., Huang, J.B., Ni, G.H., et al., 2020. Water blocking effect of coal seam based on low field nuclear magnetic resonance. J. China Coal Soc. 45 (3), 1108–1115. https://doi.org/10.13225/j.cnki.jccs.2019.1354.

Reuss, F.F., 1809. Memoirs de la societe imperiales des. Nat. de Moskou 2, 326–327 (in French).

Sang, S.X., Zhou, X.Z., Liu, S.Q., et al., 2020. Research advances in theory and technology of the stress release applied extraction of coalbed methane from tectonically deformed coals. J. China Coal Soc. 45 (7), 2531–2543. https://doi.org/10.13225/j.cnki.jccs.DZ20.0754.

Shen, B.H., Liu, J.Z., Lei, Y., 2015. Present status and prospects of coalbed methane development and utilization technology of coal mine area in China. Coal Sci. Technol. 43 (2), 1–4. https://doi.org/10.13199/j.cnki.cst.2015.02.001.

Shi, J.H., Feng, Z.C., Zhou, D., et al., 2023. Comparative study on the evolution of fracture structure of bituminous coal based on different pyrolysis methods. J. China Coal Soc. 48 (9), 3460–3470. https://doi.org/10.13225/j.cnki.jccs.2022.1330.

Song, J.X., Yu, S.Y., Su, X.B., et al., 2019. Experimental of water unlocking stimulation mechanism on surfactant fracturing fluid. Coal Geol. Explor. 47 (2), 98–102. https://doi.org/10.3969/j.issn.1001-1986.2019.02.016.

Wang, B.J., Li, M., Zhao, Q.Y., et al., 2004. Relationship between surface potential and functional groups of coals. J. Chem. Ind. Eng. (8), 1329–1334 doi: CNKI:SUN:HGSZ.0.2004-08-019.

Wang, J., Fu, X.H., Zhao, J., et al., 2016. Effect of ultra-fine grinding on coal surface properties and ultra-clean coal separation. J. China Coal Soc. 41 (6), 1524–1532. https://doi.org/10.13225/j.cnki.jccs.2015.1389.

Wittle, J.K., Hill, D.G., Chilingar, G.V., 2011. Direct electric current oil recovery (EEOR)—A new approach to enhancing oil production. Energy Sources, Part A recovery. Util. Environ. Eff. 33 (9), 805–822. https://doi.org/10.1080/15567036.2010.514843.

Wu, X., 2025. Technology and practice for efficient development of coalbed methane horizontal wells in high-rank coal of Qinshui Basin. Petrol. Reserv. Eval. Dev. 15 (2), 167–174. https://doi.org/10.13809/j.cnki.cn32-1825/te.2025.02.001.

Yang, M., Liu, L., Liu, J.J., et al., 2021. Study on joint characterization of pore structure of middle-rank coal by nitrogen adsorption-mercury intrusion-NMR. Coal Sci. Technol. 49 (5), 67–74. https://doi.org/10.13199/j.cnki.cst.2021.05.009.

Yang, Y.H., Wang, Y.T., Zhang, H., et al., 2025. Key technologies for development of typical medium-deep high-rank coalbed methane in the Qinshui Basin. Nat. Gas. Ind. 45 (7), 108–121 doi: CNKI:SUN:TRQG.0.2025-07-009.

Zeng, L., Chen, J.Y., Liu, J., et al., 2023. Study on seepage characteristics of red clay slope with fracture zone based on fluorescence tracer method. China J. Highw. Transp. 36 (3), 136–145. https://doi.org/10.19721/j.cnki.1001-7372.2023.03.010.

Zhang, B., Sun, B.L., Wang, D.Z., et al., 2024. Molecular dynamics study on the effect of minerals on the mechanical heterogeneity of anthracite coal: a case study of kaolinite in the southern part of the Qinshui Basin. J. China Coal Soc. 50 (5), 2567–2580. https://doi.org/10.13225/j.cnki.jccs.2024.0652 (in Chinese).

Zhang, B., Tao, S., Yang, F., et al., 2025. The genesis and accumulation mechanism of CBM in the typical mid- to low-rank coal-bearing basins. Pet. Sci. 22 (8), 3069–3085. https://doi.org/10.1016/j.petsci.2025.04.017.

Zhang, L.K., Kang, T.H., Kang, J.T., et al., 2020. Effects of electrolyte pH on the electro-osmotic characteristics in anthracite. ACS Omega 5 (45), 29257–29264. https://doi.org/10.1021/acsomega.0c04013.

Zhang, R., Cheng, Y.P., Yuan, L., et al., 2019. Enhancement of gas drainage efficiency in a special thick coal seam through hydraulic flushing. Int. J. Rock Mech. Min. 124, 104085. https://doi.org/10.1016/j.ijrmms.2019.104085.

Zhao, H.F., Li, P.Y., Li, X.J., et al., 2024. Fracture propagation and evolution law of indirect fracturing in the roof of broken soft coal seams. Int. J. Coal Sci. Technol. 11, 4. https://doi.org/10.1007/s40789-023-00648-8.

Zhou, L.H., Yan, X., Liu, H.T., et al., 2025. Development mechanism and practical significance of deep coalbed methane (coal rock gas) infiltration and displacement. J. China Coal Soc. 50 (7), 3534–3551. https://doi.org/10.13225/j.cnki.jccs.2025.0437.

Zhu, M.Y., Liu, Z., Yang, H., et al., 2024. Experimental and molecular dynamics study on the influence of surfactants on the wettability of different rank coal. Environ. Chem. Eng. 12 (5), 113986. https://doi.org/10.1016/j.jece.2024.113986.

Zhu, Q.Z., 2022. Key technologies and practices for efficient development of high-rank CBM in the Qinshui Basin. Nat. Gas. Ind. 42 (6), 87–96 https://doi.org/CNKI:SUN:TRQG.0.2022-06-008 (in Chinese).